journal of the mechanical behavior of biomedical materials 127 (2022) 105083

Contents lists available at ScienceDirect

Journal of the Mechanical Behavior of Biomedical Materials

journal homepage: www.elsevier.com/locate/jmbbm

Research paper

Predicting the micromechanics of embedded nerve fibers using a novel three-layered model of mouse distal colon and rectum

Yunmei Zhao [a,b,1], Bin Feng [b], David M. Pierce [a,b,*]

[a] Department of Mechanical Engineering, University of Connecticut, Storrs, CT, USA
[b] Department of Biomedical Engineering, University of Connecticut, Storrs, CT, USA

ARTICLE INFO

Keywords:
Colorectum
Three-layered model
Micromechanics
Nerve fiber
Finite element modeling
Mechanotransduction

ABSTRACT

Mechanotransduction plays a central role in evoking pain from the distal colon and rectum (colorectum) where embedded sensory nerve endings convert micromechanical stresses and strains into neural action potentials. The colorectum displays strong through-thickness and longitudinal heterogeneity with collagen concentrated in the submucosa thus indicating the significant load-bearing role of this layer. The density of sensory nerve endings is also significantly the greatest in the submucosa, suggesting a nociceptive function. Thus biomechanical heterogeneity in the colorectum influences the micromechanical stresses and strains surrounding afferent endings embedded within different layers of the colorectum which is critical for the mechanotransduction of various mechanical stimuli. In this study we aimed to: (1) calibrate and validate a three-layered computational model of the colorectum; (2) predict intra-tissue distributions of stresses and strains during mechanical stimulation of the colorectum *ex vivo* (i.e. circumferential stretching, punctuate probing, and mucosal shearing); and (3) establish a methodology to calculate local micromechanical stresses and strains surrounding afferent nerve endings embedded in the colorectum. We established three-layered FE models that include mucosa, submucosa, and muscular layers, and incorporated residual stretches, to calculate intra-tissue stresses and strains when the colorectum undergoes the mechanical stimuli used to characterize afferent neural encoding *ex vivo*. Finally, we established a methodology for detailed calculations of the local micromechanical stresses and strains surrounding afferent endings embedded in the colorectum and demonstrated this with a representative example. Our novel methodologies will bridge the existing neurophysiological and biomechanical evidence from experiments to advance our mechanistic understanding of colorectal mechanotransduction.

1. Introduction

The physiological functions of the large intestine include absorbing water, moving waste residue down the gastrointestinal (GI) tract, and temporary fecal storage, all of which involve mechanical movement and deformation of the tubular GI structure (see Siri et al., 2020 for a recent review). Visceral pain, serving as a protective mechanism, alerts us of threats and hazards in the GI tract. However, visceral pain in the absence of apparent structural damage to the GI tract is the cardinal symptom of patients with functional GI disorders and where irritable bowel syndrome (IBS) alone affects approximately 4.8% of the U.S. population (Palsson et al., 2020). IBS-related visceral pain usually initiates from the distal colon and rectum (colorectum) primarily as a result of mechanical distension/stretch rather than other thermal, mechanical, and chemical stimuli that are typically noxious, e.g., to the skin (Pasricha et al., 2006; Zhao et al., 2019).

Bulk mechanical deformation of the colorectum activates sensory (afferent) nerve endings embedded in the fibrous tissue of the colorectal wall during bowel events like peristalsis, bloating, and distension. In patients with chronic visceral pain, sensitized colorectal afferents reduce their response threshold and increase their rate of action potentials (under the same stimuli) which leads to the perception of visceral pain under normal physiological bowel events. Thus mechanotransduction, the encoding of mechanical stimuli into neural action potentials by colorectal afferent endings, is crucial to the underlying mechanisms evoking visceral pain in both health and disease (Clarke et al., 2009; Camilleri et al., 2017).

* Correspondence to: University of Connecticut, Department of Mechanical Engineering, United Technologies Engineering Building, 191 Auditorium Road Storrs, CT 06269, USA.
E-mail address: dmpierce@engr.uconn.edu (D.M. Pierce).
[1] Current affiliation: School of Aerospace Engineering and Applied Mechanics, Tongji University, Shanghai 200092, China.

https://doi.org/10.1016/j.jmbbm.2022.105083
Received 29 September 2021; Received in revised form 21 December 2021; Accepted 8 January 2022
Available online 20 January 2022

Towards understanding mechanotransduction in the colorectum, researchers focused on two categories of experimental evidence: neural encoding of mechanical stimuli and biomechanics of colorectal tissues. We and others have recorded action potentials from individual colorectal afferents via single-fiber recordings while delivering three distinct mechanical stimuli to the colorectum *ex vivo*, i.e. circumferential stretching, punctuate probing, and mucosal shearing (Brierley et al., 2004; Feng and Gebhart, 2011). This neurophysiological approach facilitated systematic characterization of mechanical neural encoding by colorectal afferents, wherein they may be classified into five major functional subtypes based upon their distinct responses to the above three mechanical stimuli: four mechanosensitive subtypes (muscular, muscular/mucosal, mucosal, and serosal afferents) and one subtype of mechanically insensitive afferents. All mechanosensitive afferents responded to punctate probing perpendicular to the colorectal wall. Muscular afferents also responded to circumferential colorectal stretching. Mucosal afferents also responded to mucosal shearing. Muscular/mucosal afferents responded to both circumferential stretching and mucosal shearing whereas serosal afferents responded to neither. Mechanically insensitive afferents responded to none of the three stimuli.

Afferents in the lumbar splanchnic nerve (LSN) dominate innervation of the colonic region and consist of four afferent subtypes (lacking only muscular/mucosal afferents). Afferents in the pelvic nerve (PN) primarily innervate the rectal region of the colorectum and include all five subtypes of afferents. PN afferents encode both low-threshold (LT) mechanical stimuli (LT circumferential stretching and mucosal shearing) and high-threshold (HT) stimuli (HT circumferential stretching and punctate probing). In contrast, most LSN afferents encode mainly HT stimuli with very few responses to LT stimuli. PN and LSN afferents appear to play differential roles in behavioral visceromotor responses (VMRs) to colorectal distension, a metric reflecting visceral pain in rodents. PN afferents facilitate the VMRs to colorectal distension in naïve mice, whereas LSN afferents dominant the VMRs in visceral hypersensitive mice induced by intracolonic treatment with irritants (e.g., trinitrobenzene sulfonic acid).

Recent studies also aimed to characterize and quantify the biomechanics of the colorectum in both macroscopic and microscopic scales. Towards these ends researchers combined mechanical tests and imaging studies to probe samples of colon tissues from animals, e.g. mice (Watters et al., 1985; Sokolis and Sassani, 2013; Gong et al., 2017; Siri et al., 2019a,b), goats (Higa et al., 2007a,b), and pigs (Qiao et al., 2005; Patel et al., 2018; Carniel et al., 2015; Puértolas et al., 2020). Leveraging mechanical tests on small tissue patches we reported distinct mechanical properties from three different longitudinal regions of the colorectum, properties consistent with the differential neural encoding properties of LSN and PN afferents that predominantly innervate colonic and rectal regions, respectively. We also separated the colorectal wall of mice into inner and outer composite layers (divided by the submucosal space) and conducted mechanical tests on these individual layers. Our tests and analyses revealed the load-bearing function of the submucosal layer within the inner composite (Siri et al., 2019a,b). Furthermore, we recently conducted through-thickness imaging of the colorectal wall via second-harmonic generation (SHG) two-photon microscopy (Maier et al., 2021). Leveraging these images we systematically characterized the distribution in orientations of collagen fibers in different layers of the colorectum. We also identified collagen fibers concentrated in the submucosal layer, data which further support the load-bearing role of the submucosa.

In the current study we focused on further advancing our mechanistic understanding of colorectal mechanotransduction by integrating experimental evidence from both afferent mechanical neural encoding and biomechanics of the colorectum. More specifically, we aimed to: (1) calibrate and validate a three-layered computational model of the colorectum; (2) predict intra-tissue distributions of stresses and strains during mechanical stimulation of the colorectum *ex vivo*, i.e. circumferential stretching, punctuate probing, and mucosal shearing; and (3) establish a methodology to calculate local micromechanical stresses and strains surrounding afferent nerve endings embedded in the colorectum. To capture the through-thickness mechanical heterogeneity of the colorectum, we established three-layered FE models that include mucosa, submucosa, and muscular layers, and incorporated residual stretches (Zhao et al., 2021b). After model validation, we conducted finite element (FE) analyses to calculate intra-tissue stresses and strains when the colorectum undergoes the mechanical stimuli used to characterize afferent neural encoding *ex vivo*. Finally, we established a methodology for calculating the local micromechanical stresses and strains surrounding afferent endings embedded in the colorectum. We demonstrated our methodology using a representative example: one afferent fiber in the submucosal layer where we determined the anatomical features using vector path tracing of previous images of optically cleared tissue (Guo et al., 2021). Our new three-layered FE model of the colorectum and our novel methodology to calculate local mechanical stresses and strains acting on individual afferent endings will bridge the existing neurophysiological and biomechanical evidence from experiments to advance our mechanistic understanding of colorectal mechanotransduction.

2. Materials and methods

2.1. Experimental evidence from mouse colorectum

We recently completed and published the following experimental studies using mouse models of the colorectum: imaging the morphology and microstructure via SHG (Maier et al., 2021), testing in biaxial extension on both bulk and layer-separated colorectal tissues (Siri et al., 2019a,b), and genetic labeling and optical clearing to image extrinsic sensory nerve fibers in bulk colorectum (Guo et al., 2021). The first two studies used the same mouse model (C57BL/6, Taconic, Germantown, NY) with mice of 8–16 weeks in age. The last study used homozygous VGLUT2-Cre mice (strain no. 28863, Jackson Laboratory, CT) crossbred with either Homozygous Ai32 mice (C57BL/6 background; strain no. 024109, The Jackson Laboratory, CT) or tdTomato mice (Ai14, strain no. 7914, The Jackson Laboratory, CT) with mice of 8–14 weeks in age.

2.1.1. Imaging via Second Harmonic Generation

We recently conducted nonlinear imaging via SHG at three different longitudinal regions of mouse colorectum (colonic, intermediate, and rectal) to quantify the morphology and dispersion of collagen fibers, as well as the thickness of each anatomic layer (Maier et al., 2021). The signal density via SHG was highest in the submucosa indicating the highest concentration of collagen fibers (per unit volume) relative to the remaining layers. Collagen fibers in the submucosa also had the highest average diameter (~5 μm) and presented two principal orientations approximately ±30° from the axial direction. Collagen fiber contents were relatively low in circular and longitudinal muscular layers as indicated by a SHG signal intensity of approximately 10% of that in the submucosal layer (Maier et al. (2021), cf. Fig. 2). The orientations of these collagen fibers in both muscular layers aligned with the muscle fibers. In contrast, collagen fibers in the mucosal layer showed no principal orientation.

In Table 1 we summarize the mean thicknesses of the mucosal, submucosal, and muscular layers at different longitudinal locations of colorectum (assuming negligible effects from residual stresses on these specific measurements). Notably the submucosal layer was relatively thin, contributing only ~20% of the wall thickness of the colorectum.

Table 1
The mean layer thicknesses for three layers (mucosa, submucosa, and muscle) for longitudinal locations (colonic, intermediate, and rectal) in the unloaded reference configurations obtained via analyses of SHG images (Maier et al., 2021).

Segment	Colonic	Intermediate	Rectal
mucosa (μm)	91.33	96.50	100.00
submucosa (μm)	30.67	41.67	58.50
muscle (μm)	37.00	46.40	70.83

2.1.2. Testing in biaxial extension

We recently performed biaxial extension tests on square specimens (7×7 mm^2) harvested from three locations along the colorectum (colonic, intermediate, and rectal) and tested these as both the bulk composite (the whole wall) and the layer-separated inner and outer composites (Siri et al., 2019a,b). Analyzing these data we determined the biaxial Cauchy stress–stretch behavior for both the bulk composite and the layer-separated inner and outer composites from colonic, intermediate, and rectal locations along the colorectum. We also quantified the nearly stress-free reference configurations of the bulk composite colorectum and the separated layers of inner and outer composites. Analyzing these data we identified the compressive and tensile residual stretches in the inner and outer composite layers respectively (Zhao et al., 2021a).

2.1.3. Vector-path tracing of nerve fibers

We recently performed genetic labeling and optical clearing to visualize extrinsic sensory nerve fibers in whole mount colorectum, which revealed widespread presence of afferent axons and endings in the submucosal layer (Guo et al., 2021). Leveraging a mouse model of IBS we genetically labeled extrinsic colorectal afferents using the promotor for vesicular glutamate transporter type 2 (VGLUT2). We systematically quantified the morphology of VGLUT2-positive axons in mouse colorectum 7–28 days following intracolonic 2,4,6-trinitrobenzenesulfonic acid (TNBS) treatment. We distended the colorectum (20 mmHg), fixed it with paraformaldehyde, and optically cleared it to image VGLUT2-positive axons throughout the colorectum. We then conducted vector path tracing of individual axons to allow systematic quantification of nerve fiber density and shape. We found that fibers in the submucosa were generally meandering and curvy, in contrast to axons in other layers generally aligned with the basal tissues.

2.2. Constitutive modeling

We considered the colorectum as a multi-layered, soft hyperelastic continuum with embedded collagen fibers. Here we extended our previous two-layered model (outer muscular–serosal composite and inner mucosal–submucosal composite), cf. Zhao et al. (2021a), by separating the inner composite into distinct mucosal and submucosal layers. To model the individual, passive mechanical responses of the layers we specified a multiplicative split of the strain–energy function Ψ into volumetric (penalized to enforce near incompressibility) and isochoric $\overline{\Psi}$ contributions as

$$\overline{\Psi} = \overline{\Psi}_{\mathrm{IM}} + \overline{\Psi}_{\mathrm{FN}}, \tag{1}$$

with $\overline{\Psi}_{\mathrm{IM}} = \mu(\bar{I}_1 - 3)/2$ as an isotropic (neo-Hookean) matrix where $\mu > 0$ is a material parameter corresponding to the shear modulus of the underlying matrix material in the reference configuration and $\bar{I}_1 = \mathrm{tr}\overline{\mathbf{C}}$ is the first invariant of $\overline{\mathbf{C}}$, the isochoric right Cauchy–Green tensor. We specified $\overline{\Psi}_{\mathrm{FN}}$, the contribution from the fiber network, as (Holzapfel et al., 2014; Pierce et al., 2016)

$$\overline{\Psi}_{\mathrm{FN}} = \int_{\Omega} \rho(\mathbf{M}) \frac{k_1}{2k_2} (\exp[k_2(\bar{I}_4 - 1)^2] - 1)\mathcal{H}(\bar{I}_4 - 1)\mathrm{d}\Omega \tag{2}$$

where $k_1 > 0$ is a stress-like material parameter, $k_2 > 0$ is a dimensionless parameter, $\bar{I}_4 = \mathbf{M} \cdot \overline{\mathbf{C}}\mathbf{M}$ is the isochoric fourth pseudo-invariant of $\mathbf{M}$ (the reference angular orientation of a single fiber), and $\mathcal{H}$ is a Heaviside function evaluated at $(\bar{I}_4 - 1)$, i.e. collagen fibers do not support compression. Finally, $\rho(\mathbf{M})$ is an orientation distribution function (ODF) characterizing the angular density of the fiber network with $1/4 \int_{\Omega} \rho(\mathbf{M})\mathrm{d}\Omega = 1$, where $\Omega = \mathbf{M} \in \mathbb{R}^3 : |\mathbf{M}| = 1$ is the unit sphere.

We specified $\rho(\mathbf{M})$ in a form inspired by, and measurable with, diffusion tensor magnetic resonance imaging (DT-MRI) which determines a second-order, symmetric, positive-definite tensor $\mathbf{D}$ (Pierce et al., 2016), i.e.

$$\rho(\mathbf{M}, \mathbf{D}) = \frac{1}{|\mathbf{D}|^{1/2}(\mathbf{M}^{\mathrm{T}}\mathbf{D}^{-1}\mathbf{M})^{3/2}}, \tag{3}$$

see Zhao et al. (2021a, Appendix A) for more details.

The mucosal layer presented relatively little collagen content without any preferred orientations and thus we modeled it using $\overline{\Psi} = \overline{\Psi}_{\mathrm{IM}}$, i.e. only the neo-Hookean strain–energy function.

2.2.1. Calibrating the model

To fit the constitutive model leveraging our data from the biaxial extension test, we wrote the invariants $I_1 = \mathrm{tr}\,\mathbf{C}$ and $I_4 = \mathbf{M} \cdot \mathbf{C}\mathbf{M}$ as

$$I_1 = \lambda_\theta^2 + \lambda_z^2 + \lambda_r^2, \tag{4}$$

and

$$I_4 = \lambda_\theta^2 \cos^2\alpha + \lambda_z^2 \sin^2\alpha, \tag{5}$$

where λ_θ and λ_z are stretches in the circumferential and longitudinal directions (considering a cylindrical coordinate system for tubular colorectum) respectively, $\lambda_r = \lambda_\theta^{-1}\lambda_z^{-1}$ (considering incompressibility), and α is the angle between the principal fiber orientation and the circumferential direction such that $D_{\theta\theta} = \cos\alpha$, $D_{zz} = \sin\alpha$, and $D_{rr} = D_{\theta z} = D_{zr} = D_{\theta r} = 0$. Considering the Cauchy stresses in the circumferential and longitudinal directions respectively as $\sigma_{\theta\theta} = \lambda_\theta(\partial\Psi/\partial\lambda_\theta)$ and $\sigma_{zz} = \lambda_z(\partial\Psi/\partial\lambda_z)$, and enforcing incompressibility $(\lambda_\theta\lambda_z\lambda_r = 1)$, we expressed the these Cauchy stresses as

$$\sigma_{\theta\theta} = 2(\lambda_\theta^2 + \lambda_\theta^{-2}\lambda_z^{-2})\Psi_1 + 2\lambda_\theta^2\cos^2\alpha\Psi_4, \tag{6}$$

and

$$\sigma_{zz} = 2(\lambda_z^2 + \lambda_\theta^{-2}\lambda_z^{-2})\Psi_1 + 2\lambda_z^2\sin^2\alpha\Psi_4, \tag{7}$$

where $\Psi_i = \partial\Psi/\partial I_i$, $i = \{1, 4\}$.

To fit our data from the inner mucosal–submucosal composite we homogenized the stresses $\sigma_{\theta\theta}$ and σ_{zz} based on relative thickness as

$$\sigma_{\theta\theta} = \beta_{\mathrm{mu}}\sigma_{\theta\theta,\mathrm{mu}} + \beta_{\mathrm{sm}}\sigma_{\theta\theta,\mathrm{sm}}, \tag{8}$$

and

$$\sigma_{zz} = \beta_{\mathrm{mu}}\sigma_{zz,\mathrm{mu}} + \beta_{\mathrm{sm}}\sigma_{zz,\mathrm{sm}}, \tag{9}$$

where $\beta_i = t_i/t$, $i = \{\mathrm{mu}, \mathrm{sm}\}$ is the thickness ratio of the mucosal and submucosal layers respectively (normalized to the total thickness of the composite t). The stresses $\sigma_{\theta\theta,i}$ and $\sigma_{zz,i}$ then follow (6) and (7). We simultaneously fit the experimental stress–stretch data for the composite mucosa–submucosa for each layer-separated specimen at each location (Siri et al., 2019b) with our constitutive model using the optimization toolbox 'lsqnonlin' in MATLAB (V2019, Mathworks, MA). We obtained four model parameters (μ, k_1, k_2, α) for the submucosa and one (μ) for the mucosa from each fitting.

2.2.2. Validating the model

We validated the predictive power of our constitutive models and modeling framework for the separated mucosa and submucosa layers by comparing results from FE analyses to independent experimental measurements from biaxial extension tests of square patches (7.0×7.0 mm^2) of intact colorectum (mucosal–submucosal–muscular bulk composite) (Siri et al., 2019b). The FE analyses for validation followed Zhao et al. (2021a). Briefly, we specified the layer thicknesses

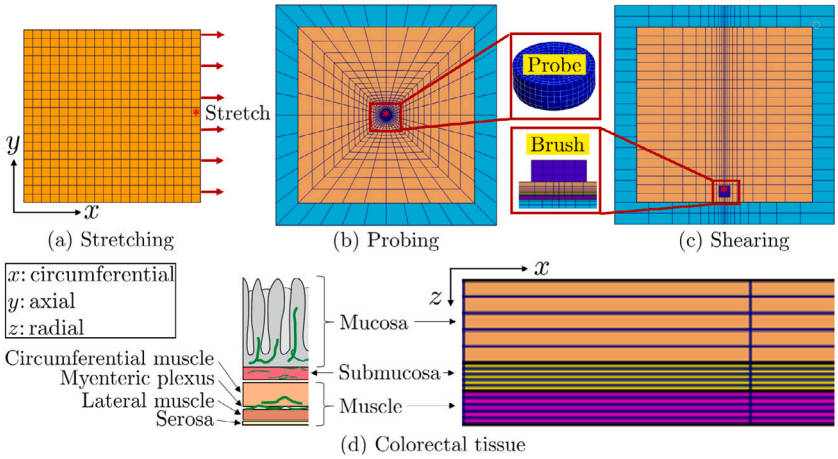

Fig. 1. Three-layered composite of colorectum — for three different mechanical stimuli, i.e. (a) stretching, (b) probing, and (c) shearing. An asterisk in each image indicates the $(x-y)$ locations of the neuron fibers (axons) embedded at the top of the submucosa within each model. (d) A schematic of the layered structure of the large intestine (left) and the corresponding representation in finite elements (right). In the Cartesian coordinate system x, y, and z denote the circumferential, axial, and radial (through-thickness) directions within the colorectum.

at each longitudinal location based on Table 1 and we incorporated residual stretches/stresses based on Zhao et al. (2021a) (Table 2), and we implemented the latter using the prestrain algorithm from FEBio (R3.0, University of Utah, UT) (Maas et al., 2012). We modeled bulk composite specimens of colorectum as three-layered, residually stressed square patches. We linearly increased the circumferential and longitudinal (axial) displacements simultaneously to model the biaxial extension tests. We completed all simulations in using FEBio.

2.3. Finite element modeling

2.3.1. Modeling the bulk-tissue mechanical stimuli

We constructed a three-layered composite colorectum to numerically reproduce the three different mechanical stimuli implemented in prior neurophysiological experiments: circumferential stretching (stretching), punctate probing perpendicular to the colorectal surface (probing), and mucosal shearing induced by genial surface stroking (shearing) (Feng and Guo, 2019); cf. Fig. 1(a)–(c). In the FE analysis we specified the layer thicknesses at each longitudinal location (colonic, intermediate, and rectal) based on Table 1, cf. Fig. 1(d). We meshed these models with eight-node hexahedral elements, and ensured relatively high mesh densities (average characteristic size laterally of 0.05 mm) at and around contact interfaces in the probing and shearing simulations. Specifically, we included at least two elements in the radial (through-thickness) direction within each (relatively thin) layer to ensure that these were not overly stiff in bending. We then used h-refinement within the circumferential–axial plane to ensure that the stress/strain results of interest changed by less than 1% upon subsequent mesh refinements. We specified the layer-specific constitutive models at each longitudinal location using our previous results for the muscle layer (Zhao et al., 2021a) and results from Section 2.2.1 for the mucosa and submucosa.

We established a three-layered square patch of colorectum with dimensions $8.0 \times 8.0\,\text{mm}^2$ to reproduce the experiments of Feng and Gebhart (2011). We separately incorporated circumferential residual stretches in the mucosal-submucosal composite (compressive) and muscular–serosal composite (tensile) in the initial configurations using the pre-stretch algorithm in FEBio (R3.0, University of Utah, UT) (Maas et al., 2012). We first predicted distributions of the circumferential residual stresses within the mucosal, submucosal, and muscular layers of bulk colorectum in the undeformed reference configuration and at three longitudinal locations.

We simulated homogeneous, circumferential stretching by fixing one edge of the patch and linearly increasing the circumferential displacements (x-direction in the figure) to a maximum of 20% stretch, see Fig. 1(a). We simulated punctate probing by pressing a cylindrical probe with a rounded edge (contact interface approximately $0.05\,\text{mm}^2$) against the mucosa surface using a frictionless contact interface. We specified the probing force as 6.25 mN, consistent with the experiments of Feng and Gebhart (2011), generating an equivalent normal stress of approximately 125 kPa on the contact surface, see Fig. 1(b). We simulated mucosal shearing (evoked by gentle surface stroking) by pressing and a relatively soft block into the mucosal surface using a contact interface with a friction coefficient of 0.02, and sliding it along this surface. We specified a contact pressure of 0.4 kPa, generating a contact area of approximately $1\,\text{mm}^2$, and prescribed the axial displacement (y-direction in the figure), see Fig. 1(c). In the probing and shearing cases we pinned the colorectum flat on a silicone foundation ($10.0\times10.0\,\text{mm}^2$) by enforcing a tied contact between the interfaces, consistent with the prior experimental conditions *ex vivo* (Feng and Gebhart, 2011; Feng and Guo, 2019).

We completed all simulations in FEBio.

2.3.2. Predicting the micromechanics of nerve fibers

We considered the curvy neuron fibers (axons) as piece-wise, microscopic cylinders embedded within a continuous fibrous matrix (Feng and Guo, 2019). To predict the stress–strain state acting on the embedded axons we defined a global Cartesian coordinate system $(\vec{E}_x, \vec{E}_y, \vec{E}_z)$ with Cauchy stress tensor $\boldsymbol{\sigma}$ and Green–Lagrange strain tensor $\mathbf{E}$ characterizing the local mechanical conditions within the macroscopic fibrous tissue, see Fig. 2. We further assumed that each piece-wise cylinder had homogeneous stress and strain distributions in response to loading of the bulk tissue. Thus we labeled the orientation of ith cylinder using its axial vector $\vec{n}$ (see Fig. 2(a)) with respect to the $\vec{E}_x, \vec{E}_y, \vec{E}_z$ coordinates, and transformed to a local Cartesian coordinate system $(\vec{i}_x, \vec{i}_y, \vec{i}_z)$ using Euler angles $\beta \in [0, 360°)$ and $\gamma \in [0, 180°)$, with $\vec{n}$ parallel to $\vec{i}_z$. Furthermore, with the intention of acquiring the normal stress (out-of-plane) and shear stress (in-plane) acting on the outer nerve membrane, we defined a local cylindrical coordinate system $(\vec{a}_r, \vec{a}_\theta, \vec{a}_z)$ within each cylinder, with $\vec{a}_z$ parallel to $\vec{i}_z$, see Fig. 2(b). Here $\theta \in [0, 360°)$ in the microscopic reference system denotes all possible projections normal to the cylindrical segment at a specific z coordinate.

Following Cauchy's Law (Spencer, 2004), we expressed the (microscale) stress tensor $\boldsymbol{\sigma}'$ acting on the outer nerve membrane as a transformation of the local macroscale stress $\boldsymbol{\sigma}$, i.e. $\boldsymbol{\sigma}' = \mathbf{Q}\,(\mathbf{T}\,\boldsymbol{\sigma}\,\mathbf{T}^{\mathrm{T}})\,\mathbf{Q}^{\mathrm{T}}$, where

$$\mathbf{T} = \begin{bmatrix} \cos\gamma & \sin\gamma\sin\beta & \cos\beta\sin\gamma \\ 0 & \cos\beta & -\sin\beta \\ -\sin\gamma & \sin\beta\cos\gamma & \cos\beta\cos\gamma \end{bmatrix} \tag{10}$$

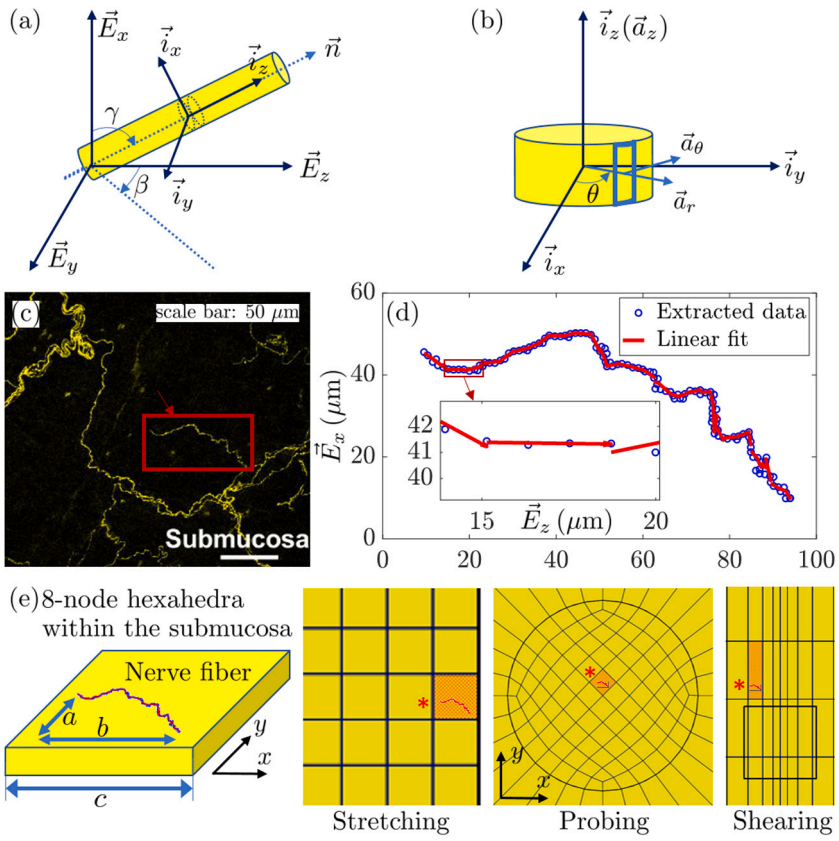

Fig. 2. Calculating the local (microscopic) normal stress (out-of-plane) and shear stress (in-plane) acting on the outer nerve membrane embedded in the colorectum. (a) Schematic of a cylindrical segment of nerve fiber with relevant coordinate systems: global Cartesian ($\vec{E}_x, \vec{E}_y, \vec{E}_z$) and cylinder-dependent local Cartesian ($\vec{i}_x, \vec{i}_y, \vec{i}_z$). (b) Schematic of inset cylindrical segment with cylindrical coordinates ($\vec{a}_r, \vec{a}_\theta, \vec{a}_z$). (c) Representative example of methodology focuses on a curvy nerve fiber in the submucosa (highlighted by the box with arrowhead) imaged via confocal microscopy (Guo et al., 2021). (d) Representative piece-wise linear fitting of the highly undulated nerve fiber, shown as the composition of 41 line segments and modeled as a series of cylinders. (e) A representative schematic of a finite element with embedded nerve fiber where $a < 50\,\mu m$, $b < 100\,\mu m$, and $c \approx 100 - 400\,\mu m$ (left) and magnified images of the elements within the submucosa of each model (right). An asterisk in each image indicates the $(x - y)$ locations of the neuron fibers (axons) embedded at the top of the submucosa within each model, cf. Figs. 1(a)–(c).

maps the transformation from $\vec{E}_i$ to $\vec{i}_k$, and where

$$\mathbf{Q} = \begin{bmatrix} \cos\theta & \sin\theta & 0 \\ -\sin\theta & \cos\theta & 0 \\ 0 & 0 & 1 \end{bmatrix} \tag{11}$$

maps the transformation from $\vec{i}_k$ to $\vec{a}_j$. We transform Green–Lagrange strain tensor $\mathbf{E}$ similarly to calculate the (microscale) strain tensor $\mathbf{E}'$.

To demonstrate our full methodology we selected, as a representative example, a specific curvy nerve fiber in the submucosa previously imaged via confocal microscopy, see Fig. 2(c) (Guo et al., 2021). This nerve fiber (highlighted by the box with arrowhead) within the submucosa, presents a diameter of approximately 1 μm. We defined Cartesian coordinates to capture the geometric characteristics of the nerve fiber we selected. We extracted the undulating features of the nerve fiber from the microscopy image as a set of points (x_l, y_l) along the fiber using the image-analysis tool Webplotdigitize (Drevon et al., 2017), and then reconstructed its curvy appearance, see Fig. 2(d). We fit this series of points with piece-wise lines while maintaining the fitting error $\left|(f(x_l) - y_l)/y_l\right| < 5\%$, in which $f(x_l)$ is the fitted results for each data point. Finally, we reconstructed the nerve fiber as a series of interconnected cylinders (∅ 1 μm), one cylinder for each line segment from the piece-wise linear fitting, thus approximating the complete crimped path of a specific fiber within the submucosa. In this representative example (the nerve fiber selected in Fig. 2(c)) measured 156.8 μm in length and we implemented 41 linear segments. We assumed that the nerve fibers lay in the x–y plane at the top ($z = z_{min}$) of the submucosa and centered in the bottom ($y = y_{min}$) third of the element specified, see Fig. 2(e) and Figs. 1(a)–(c). To visualize the peak normal stresses/strains (out-of-plane) and shear stresses/strains (in-plane) acting on the embedded, cylindrical surface we plotted them both as a function of $\theta \in [0, 360°)$ at the first cylindrical segment and as a function of the length ∈ [0, 156.8 μm] (with mean values over θ).

Table 2
Model parameters for the mucosa and the submucosa of the colorectum.

Segment	μ (kPa)	k_1 (kPa)	k_2 (-)	α (-)
Mucosa Colonic	29.16	–	–	–
Mucosa Intermediate	19.95	–	–	–
Mucosa Rectal	14.98	–	–	–
Submucosa Colonic	47.43	63.41	34.56	60.10
Submucosa Intermediate	32.97	102.9	18.90	50.14
Submucosa Rectal	21.73	83.54	26.95	46.45

3. Results

3.1. Constitutive modeling

3.1.1. Calibrating the model

Our constitutive model and homogenized calibration method was able to successfully fit experimental data from biaxial stretching of the mucosa–submucosa composite for each longitudinal location, i.e. colonic, intermediate, and rectal (not shown). Table 2 summarizes the resulting model parameters for both the mucosa and the submucosa at different longitudinal locations.

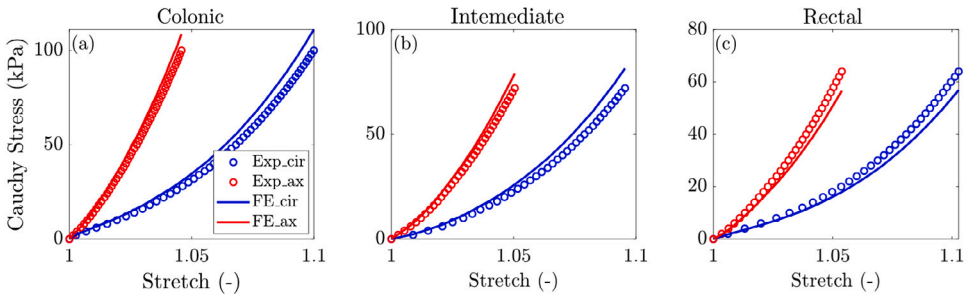

Fig. 3. Model validation: mean experimental data (circles) with corresponding model predictions (solid curves) for (a) colonic, (b) intermediate, and (c) rectal bulk composite specimens of colorectum undergoing biaxial extensions. EXP = EXPeriment, FE = Finite Element Analyses, cir = Circumferential, and ax = Axial.

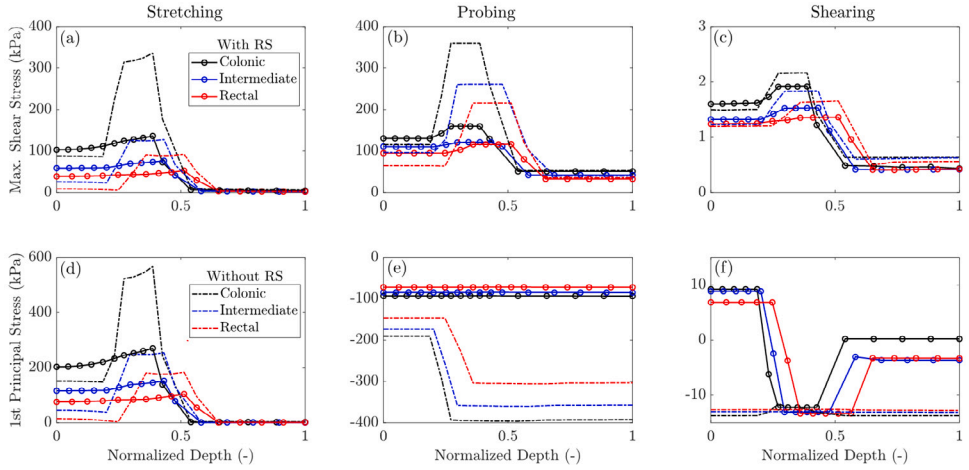

Fig. 4. Predicted distributions of both maximum shear stresses (a)–(c) and first principal stresses (d)–(e) through the normalized thickness (mucosa, submucosa, and muscular layers) of the deformed wall undergoing (a), (d) stretching; (b), (e) probing; and (c), (f) shearing; where 0 denotes the outer serosal surface and 1 the inner mucosal surface. Predictions presented both with (curves with circles) and without (dashed curves) including residual stresses (RS).

Table 3
Predicted distributions of the circumferential residual stresses within the mucosal, submucosal, and muscular layers of bulk colorectum in the undeformed reference configuration.

Segment	Colonic (kPa)	Intermediate (kPa)	Rectal (kPa)
Mucosa	−0.96	−0.74	−0.65
Submucosa	−4.07	−2.82	−2.46
Muscular	10.34	7.99	6.74

3.1.2. Validating the model

Fig. 3 presents the simulated biaxial extension tests (FE model of the reconstructed three-layered, bulk composite specimen using the mean model parameters, cf. Table 2 and Zhao et al. (2021a)) against the mean experimental results for the bulk composite colorectum quantified independently (Siri et al., 2019a,b).

3.2. Finite element modeling

3.2.1. Modeling the bulk-tissue mechanical stimuli

Table 3 summarizes the predicted distributions of the circumferential residual stresses within the mucosal, submucosal, and muscular layers of bulk colorectum in the undeformed reference configuration and at three longitudinal locations.

Fig. 4 presents the predicted distributions of both maximum shear stresses (Fig. 4(a)–(c)) and first principal stresses (Fig. 4(d)–(e)) through the normalized thickness (mucosa, submucosa, and muscular layers) of the deformed wall undergoing stretching (a), (d); probing (b), (e); and shearing (c), (f); where 0 denotes the outer serosal surface and 1 the inner mucosal surface.

3.2.2. Predicting the micromechanics of nerve fibers

Figs. 5–7 present the representative distributions of Cauchy stresses and Green–Lagrange strains surrounding the embedded neuron fibers within the submucosa in response to mechanical stimuli of circumferential stretching (Fig. 5), punctate probing (Fig. 6), and mucosal shearing (induced by genial surface stroking, Fig. 7).

4. Discussion

4.1. Constitutive modeling

Combining our experimental observations, i.e. the mechanical responses quantified with biaxial testing (both bulk composite and layer separated) and the layer-specific distributions of collagen quantified via SHG, we improved the fidelity of our simulations of the colorectum by establishing a three-layered, mucosal–submucosal–muscular computational model, see Fig. 3. The inner and outer composite layers from our previous modeling of the colorectum were themselves heterogeneous through the thickness (Zhao et al., 2021a), thus motivating part of the current work. Specifically, the mucosa and submucosa have different physiological functions and present very different constitutions and microstructures. We sought to model these as two individual layers, cf. Table 2.

We based the constitutive model we established for the submucosa in part on tissue-level information from histology and microscopy, allowing us to associate the material parameters with the microstructural arrangement of collagen fibers. Based on the imaging analyses, we directly computed the required diffusion tensors via the experimentally measured angles α, defined as the principal orientation of fiber reinforcement with respect to the circumferential direction. In future

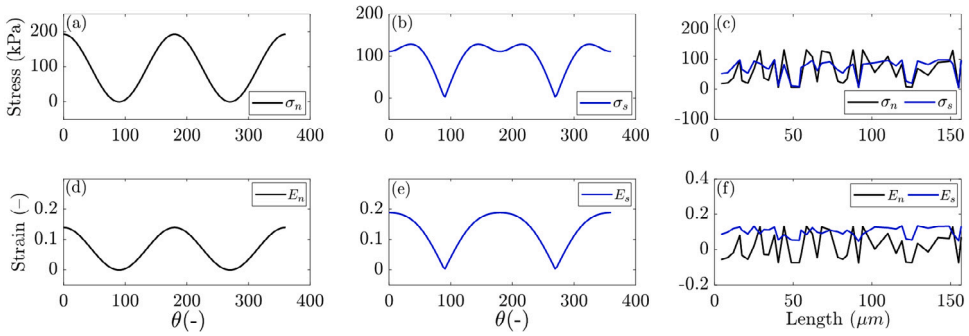

Fig. 5. Predicted distributions of Cauchy stresses and Green–Lagrange strains acting on the surface of the embedded neuron fibers within the submucosa in response to circumferential stretching: (out-of-plane) normal components (a) σ_n and (d) E_n and (in-plane) shear components (b) σ_s and (e) E_s as a function of $\theta \in [0, 360°)$ at the first cylindrical segment; and the averaged distributions of these (c) stresses and (f) strains along entire length ∈ [0, 156.8 μm] of the representative fiber, cf. Fig. 2(c) (Guo et al., 2021).

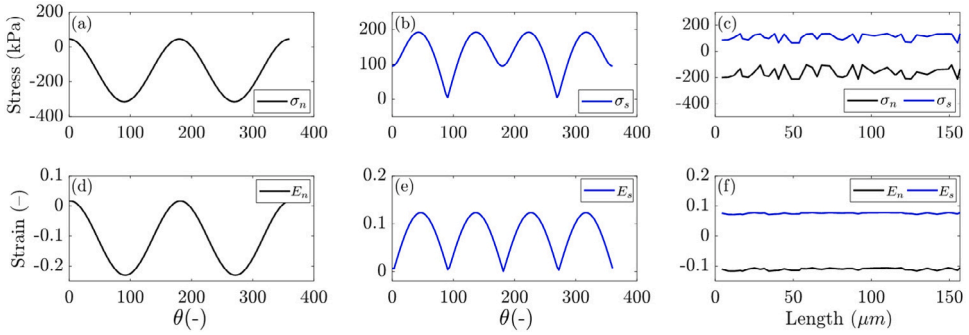

Fig. 6. Predicted distributions of Cauchy stresses and Green–Lagrange strains acting on the surface of the embedded neuron fibers within the submucosa in response to punctate probing: (out-of-plane) normal components (a) σ_n and (d) E_n and (in-plane) shear components (b) σ_s and (e) E_s as a function of $\theta \in [0, 360°)$ at the first cylindrical segment; and the averaged distributions of these (c) stresses and (f) strains along entire length ∈ [0, 156.8 μm] of the representative fiber, cf. Fig. 2(c) (Guo et al., 2021).

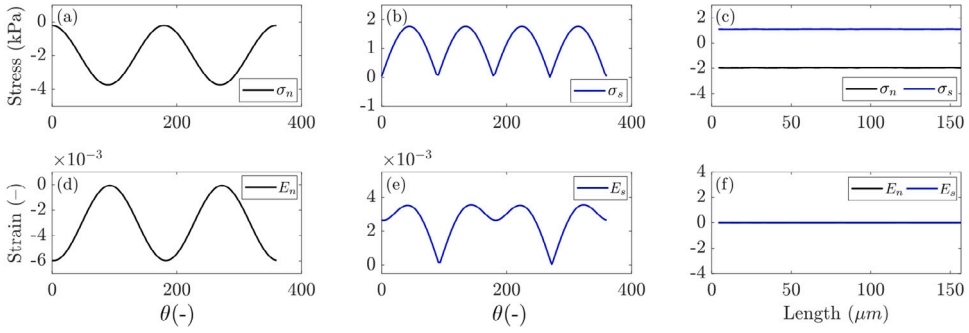

Fig. 7. Predicted distributions of Cauchy stresses and Green–Lagrange strains acting on the surface of the embedded neuron fibers within the submucosa in response to mucosal shearing: (out-of-plane) normal components (a) σ_n and (d) E_n and (in-plane) shear components (b) σ_s and (e) E_s as a function of $\theta \in [0, 360°)$ at the first cylindrical segment; and the averaged distributions of these (c) stresses and (f) strains along entire length ∈ [0, 156.8 μm] of the representative fiber, cf. Fig. 2(c) (Guo et al., 2021).

applications of the constitutive model these diffusion tensors could be directly measured and implemented into FE models.

Our fitted model (Table 2) showed strong mechanical heterogeneity though the thickness of the colorectal wall, and indicated that although the mucosal layer occupies the thickest portion of the wall, the relatively thin submucosa presents strong reinforcement with collagen and is therefore the principal load-bearing structure of the inner composite. On a microscopic scale, the two prominent orientations of fibers (two families) form a dispersed network in the submucosa that informs the micromechanical environment therein, an environment that is heavily innervated by sensory nerve endings (Guo et al., 2021). Thus the distribution and alignment of collagen may play an important role in modulating the mechanical stimulation reaching the embedded nerve fibers.

4.2. Finite element modeling

4.2.1. Modeling the bulk-tissue mechanical stimuli

Table 3 summarizes the predicted distributions of the circumferential residual stresses within the mucosal, submucosal, and muscular layers of bulk colorectum in the undeformed reference configuration and at three longitudinal locations. These residual stresses arise in response to the residual stretches, based on experimental measurements, applied to the model. In the physiological state, the inner mucosa and submucosa is in compression circumferentially, while the outer muscular layer is in tension.

Fig. 4 compares the (macroscopic) tissue-level distributions of stresses through the thickness of the colorectum, and it demonstrates relatively high magnitudes of both shear and first principal stresses within the thin submucosa layer as compared to those in the mucosal and muscular layers. This finding is consistent with our image-based

observations of the fibrous collagen content (Maier et al., 2021), as well as our modeling fitting results, cf. Section 3.1.1. In particular, we noticed that the connective submucosal and muscular layers bear comparable stresses to those in the bulk colorectum while undergoing the three mechanical stimuli (stretching, probing, and shearing), while the (thickest) mucosal layer generally bears relatively low stresses within the bulk tissue. Additionally, the magnitudes of stresses decrease from proximal, colonic location to the distal, rectal location, also consistent with the longitudinal heterogeneity of the tissue properties (Siri et al., 2019a; Zhao et al., 2021a).

Our simulation results clearly indicate that circumferential residual stresses play a crucial role in attenuating the gradient in stresses at the mucosal–submucosal interface, i.e. increasing the stress at the muscular layers by tensile residual stresses while decreasing the stresses at the submucosal layers by compressive residual stresses. Since the composite mucosa–submucosa presents nonlinear stress–strain responses, relatively small magnitudes of residual stresses in the unloaded configuration may result in pronounced changes in the stresses under external mechanical stimuli, as revealed in Fig. 4. Overall the residual stresses likely reduce the likelihood of damaging the submucosa as the bulk composite tissue undergoes applied mechanical loading.

Reviewing the three external mechanical stimuli we simulated, we found that perpendicular probing leads to the most severe state of stresses through the wall thickness, as compared to the other two types of stimuli. Circumferential stretching of an $8.0 \times 8.0\,mm^2$ patch of mouse colorectum with a force of up to 170 mN recapitulates the circumferential colorectal distension present as the intact, tubular colorectum undergoing pressure loading up to ~50 mmHg (Feng and Gebhart, 2011). Such loading is beyond the noxious threshold of 20 mmHg in mice. Similarly, our simulations of probing generate focal stresses comparable to injurious colorectal distension beyond at least 80 mmHg (Feng and Gebhart, 2011). Therefore, the stretching and probing conditions we simulated are noxious and similar loading *in vivo* may evoke nociceptive responses.

4.2.2. Predicting the micromechanics of nerve fibers

Nerve fibers within the submucosa are extremely narrow and highly crimped (Guo et al., 2021). We estimated the microscale stresses and strains acting on a nerve fiber embedded within the submucosa by decomposing the curvy fiber into a piece-wise series of cylinders, and calculated the micromechanics surrounding each cylindrical segment by leveraging the results of our FE simulations of bulk composite tissues undergoing external mechanical loads (stretching, probing, and shearing). Due to symmetry in the individual cylindrical segments, stresses and strains acting on the cylinders are periodic when plotted versus the angle θ from 0 to 360°. Specifically, Figs. 5–7(a, d) presented the in-plane (shearing) stresses (σ_s) and strains (E_s) acting on the first segment of the nerve membrane while Figs. 5–7(b, e) presented the out-of-plane (normal) stresses (σ_n) and strains (E_n). Meanwhile, Figs. 5–7(c, f) presented the average stresses and strains (averaged over the angle θ) acting on the nerve membrane along the length of the curvy fiber (see Fig. 2(c)). Fig. 2(d) presented 41 segments where the abscissa of Figs. 5–7(c, f) is the accumulated length of the piece-wise cylinders.

In our simulation results for circumferential stretching (Fig. 5) the positive normal and shear stresses/strains indicated that the beginning of the fiber membrane undergoes distension. We also found that complete nerve fibers have comparable averaged stress and strain distributions along their lengths. In our results for probate probing (Fig. 6) the beginning of the fiber membrane undergoes compressive normal stresses but positive shear stresses, and the averaged components also have comparable magnitudes. In our results for surface stroking (shearing) (Fig. 7) the stress and strain values are similar in distribution to those in probing (Fig. 6) but with much lower magnitudes reflecting the vast difference in intensity of the stimuli between probing and shearing.

Our simulation results demonstrate the mechanical responses of fibrous colorectum tissues to specific mechanical stimuli, and how these responses may modulate the mechanical environment of neuron. On the macroscale, owing largely to the dispersed organization of collagen, mechanical stimuli cause heterogeneous and localized stress distributions. In our microscale stress and strain analyses we predicted that the application of mechanical loads to bulk (intact) colorectum would lead to progressive deformation of the nerve fiber, deformation which may lead to activation of stretch-sensitive ion channels embedded in the afferent membrane and subsequent generation of action potentials that inform the central nervous system. Nerve fibers embedded within the colorectal tissue may activate under injurious mechanical loading, loading that leads to visceral nociception and visceral pain.

4.3. Limitations and outlook

After refining our multi-layered model of the colorectum we analyzed the transmission of external mechanical loading, i.e. stretching, probing, and shearing, from within the bulk tissue to the embedded neurons (in a representative example). We acknowledge several limitations of our study. We neglected active smooth muscle tone in our modeling consistent with prior neurophysiological recordings from sensory afferents in which L-type calcium channel blocks inhibited smooth muscle tone in the colorectum. Future experimental and computational studies on colorectal mechanotransduction could consider smooth muscle contractility which may potentially contribute to visceral pain in IBS. Our methodology considered the nerve fibers as embedded in the fibrous extracellular matrix, and assumed a constant, cylindrical cross-section to predict the local stresses and strains acting on the nerve fiber. We note that the modeling scheme is purely based on continuum mechanics (and is not multi-scale) and thus we assume that the nerve fibers are sufficiently small that they do not effect the local state of stress and strain. Our methodology can predict the microscale mechanical stresses and strains acting on individual nerve fibers, but our results are not supported by any experimental evidence. The lack of relevant experimental evidence both highlights the major (current) limitations of this field of research (experimental identification of cell-scale deformations in bulk biological tissues) and provides rationale for our proposed computational methodology.

Our simulations capture biomechanical heterogeneity across both the longitudinal and through-thickness directions of the colorectum, highlighting the differential roles of sensory nerve endings in different regions of the colorectum in visceral mechanotransduction. Our proposed three-layered, modeling framework and the procedure for deriving microscale stress and strain in individual fibers improve our knowledge of mechanical heterogeneity of the colorectum. Our finite element simulations of intra-tissue stresses/strains within the three-layered colorectum will inform models that explore the local stress/strain stimuli at the individual afferent nerve endings. Future analyses of the macro- and micro-mechanics may help to identify key components in triggering neural responses to visceral mechanical stimuli in both health and disease. Such analyses will allow further integration of data on tissue biomechanics with functions of afferent neural encoding from neurophysiological recordings to facilitate mechanistic understanding of colorectal mechanotransduction and mechano-nociception. Our combined experimental and computational modeling approach will quantitatively determine the contribution of biomechanical factors on sensitization of colorectal afferents, especially “biomechanical" sensitization of afferents in the load-bearing submucosa that potentially drives prolonged visceral pain in IBS patients in the absence of any apparent biological and immunological abnormalities.

CRediT authorship contribution statement

Yunmei Zhao: Conceptualization, Data curation, Formal analysis, Investigation, Methodology, Software, Validation, Visualization, Writing – original draft, Writing – review & editing. **Bin Feng:** Writing – review & editing, Writing – original draft, Visualization, Validation,

Supervision, Resources, Project administration, Methodology, Investigation, Funding acquisition, Formal analysis, Data curation, Conceptualization. **David M. Pierce:** Writing – review & editing, Writing – original draft, Visualization, Validation, Supervision, Software, Resources, Project administration, Methodology, Investigation, Funding acquisition, Formal analysis, Data curation, Conceptualization.

Declaration of competing interest

The authors declare that they have no known competing financial interests or personal relationships that could have appeared to influence the work reported in this paper.

Acknowledgments

This material stems from research supported by National Science Foundation, United States 1727185 and National Institutes of Health, United States 1R01DK120824-01.

References

Brierley, S.M., Jones, III, R.C.W., Gebhart, G.F., Blackshaw, L.A., 2004. Splanchnic and pelvic mechanosensory afferents signal different qualities of colonic stimuli in mice. Gastroenterology 127, 166–178.

Camilleri, M., Halawi, H., Oduyebo, I., 2017. Biomarkers as a diagnostic tool for irritable bowel syndrome: where are we? Expert Rev. Gastroenterol. Hepatol. 11, 303–316.

Carniel, E., Gramigna, V., Fontanella, C., Frigo, A., Stefanini, C., Rubini, A., Natali, A., Characterization of the anisotropic mechanical behaviour of colonic tissues: experimental activity and constitutive formulation. Exp. Physiol. 99, 759–771.

Carniel, E.L., Mencattelli, M., Bonsignori, G., Fontanella, C.G., Frigo, A., Rubini, A., Stefanini, C., Natali, A.N., 2015. Analysis of the structural behaviour of colonic segments by inflation tests: experimental activity and physio-mechanical model. Proc. Inst. Mech. Eng. H 229, 794–803.

Clarke, G., Quigley, E.M., Cryan, J.F., Dinan, T.G., 2009. Irritable bowel syndrome: towards biomarker identification. Trends Mol. Med. 15, 478–489.

Drevon, D., Fursa, S.R., Malcolm, A.L., 2017. Intercoder reliability and validity of webplotdigitizer in extracting graphed data. Behav. Modif. 41, 323–339.

Feng, B., Gebhart, G.F., 2011. Characterization of silent afferents in the pelvic and splanchnic innervations of the mouse colorectum. Am. J. Physiol. Gastrointest. Liver Physiol. 300, G170–G180.

Feng, B., Guo, T., 2019. Visceral pain from colon and rectum: The mechanotransduction and biomechanics. J. Neural Transm. 1–15.

Gong, X., Xu, X., Lin, S., Cheng, Y., Tong, J., Li, Y., 2017. Alterations in biomechanical properties and microstructure of colon wall in early-stage experimental colitis. Exp. Ther. Med. 14, 995–1000.

Guo, T., Patel, S.P., Shah, D., Chi, L., Emadi, S., Pierce, D.M., Han, M., Brumovsky, P.R., Feng, B., 2021. Optical clearing reveals tnbs-induced morphological changes of vglut2-positive nerve fibers in mouse colorectum. Am. J. Physiol. Gastrointest. Liver Physiol..

Higa, M., Luo, Y., Okuyama, T., Shiraishi, Y., Liu, H., Yambe, T., Takagi, T., 2007a. In vivo measurements and constitutive modeling of colon tissue. In: World Congress on Medical Physics and Biomedical Engineering. Springer, pp. 3186–3189.

Higa, M., Luo, Y., Okuyama, T., Takagi, T., Shiraishi, Y., Yambe, T., 2007b. Passive mechanical properties of large intestine under in vivo and in vitro compression. Med. Eng. Phys. 29, 840–844.

Holzapfel, G.A., Unterberger, M.J., Ogden, R.W., 2014. An affine continuum mechanical model for cross-linked f-actin networks with compliant linker proteins. J. Mech. Beh. Biomed. Mat. 38, 78–90.

Maas, S.A., Ellis, B.J., Ateshian, G.A., Weiss, J.A., 2012. Febio: finite elements for biomechanics. J. Biomech. Eng. 134.

Maier, F., Siri, S., Santos, S., Chen, L., Feng, B., Pierce, D.M., 2021. The heterogeneous morphology of networked collagen in distal colon and rectum of mice quantified via nonlinear microscopy. J. Mech. Beh. Biomed. Mat. 113, 104116.

Palsson, O., Whitehead, W., Törnblom, H., Sperber, A., Simren, M., 2020. Prevalence of rome IV functional bowel disorders among adults in the united states, canada, and the united kingdom. Gastroenterology 158, 1262–1273.e3.

Pasricha, P.J., Willis, W.D., Gebhart, G.F., 2006. Chronic Abdominal and Visceral Pain: Theory and Practice. Taylor & Francis, US.

Patel, B., Chen, H., Ahuja, A., Krieger, J.F., Noblet, J., Chambers, S., Kassab, G.S., 2018. Constitutive modeling of the passive inflation-extension behavior of the swine colon. J. Mech. Beh. Biomed. Mat. 77, 176–186.

Pierce, D.M., Unterberger, M.J., Trobin, W., Ricken, T., Holzapfel, G.A., 2016. A microstructurally based continuum model of cartilage viscoelasticity and permeability incorporating measured statistical fiber orientations. Biomech. Model. Mechanobiol. 15, 229–244.

Puértolas, S., Peña, E., Herrera, A., Ibarz, E., Gracia, L., 2020. A comparative study of hyperelastic constitutive models for colonic tissue fitted to multiaxial experimental testing. J. Mech. Beh. Biomed. Mat. 102, 103507.

Qiao, Y., Pan, E., Chakravarthula, S., Han, F., Liang, J., Gudlavalleti, S., 2005. Measurement of mechanical properties of rectal wall. J. Mater. Sci. Mater. Med. 16, 183–188.

Siri, S., Maier, F., Chen, L., Santos, S., Pierce, D.M., Feng, B., 2019a. Differential biomechanical properties of mouse distal colon and rectum innervated by the splanchnic and pelvic afferents. Am. J. Physiol. Gastrointest. Liver Physiol. 316, G473–G481.

Siri, S., Maier, F., Santos, S., Pierce, D.M., Feng, B., 2019b. Load-bearing function of the colorectal submucosa and its relevance to visceral nociception elicited by mechanical stretch. Am. J. Physiol. Gastrointest. Liver Physiol. 317, G349–G358.

Siri, S., Zhao, Y., Maier, F., Pierce, D., Feng, B., 2020. The macro- and micro-mechanics of the colon and rectum I: Experimental evidence. Bioengineering 7 (130).

Sokolis, D.P., Sassani, S.G., 2013. Microstructure-based constitutive modeling for the large intestine validated by histological observations. J. Mech. Beh. Biomed. Mat. 21, 149–166.

Spencer, A.J.M., 2004. Continuum Mechanics. Courier Corporation.

Watters, D., Smith, A., Eastwood, M., Anderson, K., Elton, R., 1985. Mechanical properties of the rat colon: the effect of age, sex and different conditions of storage. Q. J. Exp. Physiol. 70, 151–162.

Zhao, J., Liao, D., Gregersen, H., 2019. Mechanical analysis of intestinal contractility in a neonatal maternal deprivation irritable bowel syndrome rat model. J. Biomech. 93, 42–51.

Zhao, Y., Siri, S., Feng, B., Pierce, D., 2021a. Computational modeling of mouse colorectum capturing longitudinal and through-thickness biomechanical heterogeneity. J. Mech. Beh. Biomed. Mat. 113, 104127.

Zhao, Y., Siri, S., Feng, B., Pierce, D., 2021b. Toward elucidating the physiological impacts of residual stresses in the colorectum. J. Biomech. Eng. 144, 011008.